Supplementary Information for "Stabilization and Adiabatic Control of Antiferromagnetically Coupled Skyrmions without Topological Hall Effect"

Rawana Yagan[1], Arash Mousavi Cheghabouri[1], Mehmet C. Onbasli[1,2]

[1]Department of Electrical and Electronics Engineering, Koç University, Sarıyer, Istanbul 34450, Turkey
[2]Department of Physics, Koç University, Sarıyer, Istanbul 34450, Turkey

Table of Contents

Figure List

Video List

Supplementary Video V10. smooth.out (not sidewall roughness)
Supplementary Video V11. rough_edges10.out (sidewall roughness: $\mathcal{N}(0,\ 10\%\times$channel width))
Supplementary Video V12. rough_edges20.out ($\mathcal{N}(0,\ 20\%\times$channel width))
Supplementary Video V13. rough_edges40.out ($\mathcal{N}(0,\ 40\%\times$channel width))

$\mathcal{N}(0,\ 2\%\times K_u^0)$) stands for a Gaussian random variable with 0 mean and $2\%\times K_u^0$ standard deviation

1. SAF skyrmion at finite temperature

The results in Figures S1 and S2 are from the simulations for the SAF skyrmions with the set of parameters mentioned in the methods section of the main manuscript. Here, we add the effect of temperature on the micromagnetic models of the skyrmion behavior. The temperature effects are included in the micromagnetic models are based on the stochastic effective field terms as described in references [1, 2]. Figures S1(a) and S1(b) below show the equilibrated SAF skyrmion at T = 0 K and 100 K, respectively. In Figure S1(a) the relaxed skyrmion has a radius of 22 nm. In Figure S1(b) the skyrmions keeps growing showing instability even after running the simulation for 5 ns.
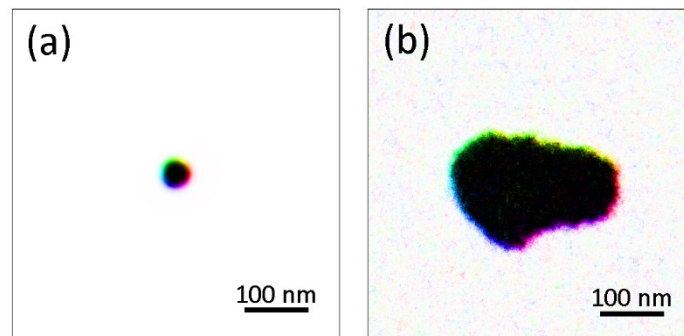
Figure S1. SAF skyrmion (showing top interface) at (a) 0 K and (b) 100 K temperature fields.

The temperature effects can be overcome by raising the effective anisotropy barrier of the coupled SAF skyrmions. To raise this barrier, uniaxial anisotropy constant can be the primary solution that can be used for stabilization of the SAF skyrmions. Once the K_u is increased, the external magnetic field could also be added for further enhancing this total effective anisotropy barrier.

1.1 Uniaxial anisotropy and external applied field B_z effects on SAF skyrmion at finite temperature

We present in Figure S2 the effect of uniaxial magnetocrystalline anisotropy on the SAF skyrmion in one of the interfaces as we apply the temperature field T = 100 K. We observe that in Figure S2(a) at $K_u = 85 \times 10^4$ J/m^3 even after running the simulation some time (5 ns) the skyrmion keeps on growing showing instability while in (b) at a larger $K_u = 95 \times 10^4$ J/m^3 the skyrmion preserves its size and shape. In Figures S2(c) and (d), we apply the field $B_z = 70$ mT (not enough to decouple the SAF skyrmion pair) for both K_u values and we observe a distortion in the shape of the skyrmion for both cases. The applied field should not be too high to decouple the SAF skyrmions.
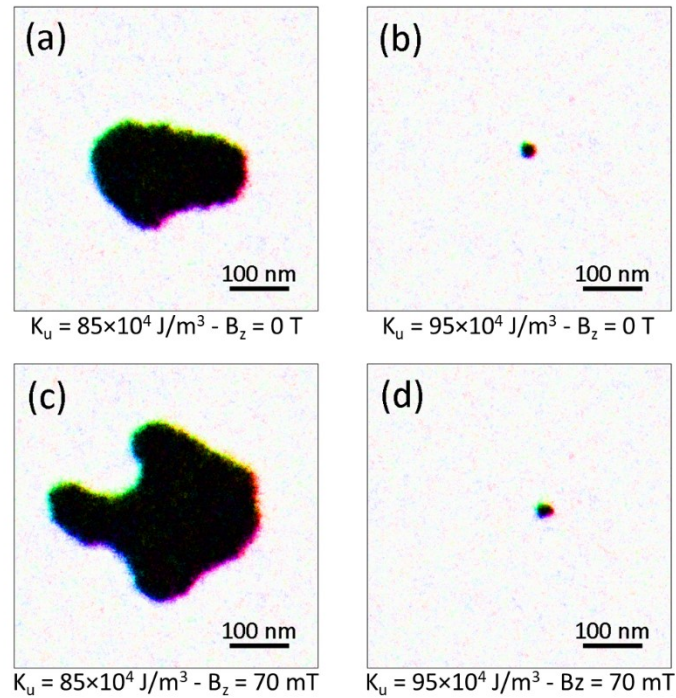
Figure S2. Effect of uniaxial anisotropy on the SAF skyrmion at finite temperature. MuMax3 simulation outputs of SAF skyrmion at T = 100 K at (a) $K_u = 85 \times 10^4$ J/m^3 and $B_z = 0$ T, (b) $K_u = 95 \times 10^4$ J/m^3 and $B_z = 0$ T, (c) $K_u = 85 \times 10^4$ J/m^3 and $B_z = 70$ mT, and (d) $K_u = 95 \times 10^4$ J/m^3 and Bz = 70 mT.

2. The Effect of Interlayer Exchange Coefficient (J_{int}) and the Out-of-plane Applied Magnetic Field (B_z) on The SAF Skyrmion Radius at Equilibrium

Figure 4(a) in the main manuscript shows the effect of increasing external applied magnetic field (B_z) on the radii of the top and the bottom coupled SAF skyrmions. The Figure (b) in the main manuscript shows the effect of J_{int} (interlayer exchange constant) and the magnetic field on the radius difference of the coupled SAF skyrmions.

In Figure S3, we show the effect of B_z and J_{int} on the radius of the skyrmion on the bottom interface. Applied B_z field causes opposite signs of contributions to the effective magnetic anisotropy field of the top and the bottom SAF skyrmions. Below a threshold of J_{int} magnitude and at larger fields, the skyrmions are no longer coupled and the bottom skyrmion shrinks with the field independently from the top skyrmion. As a result, the bottom skyrmion shrinks with increasing field for a constant J_{int}, while the top skyrmion enlarges with increasing field for a constant J_{int}. The radius of the top skyrmion can be found by adding the Figure 4(b) data of the main manuscript with those of Figure S3.
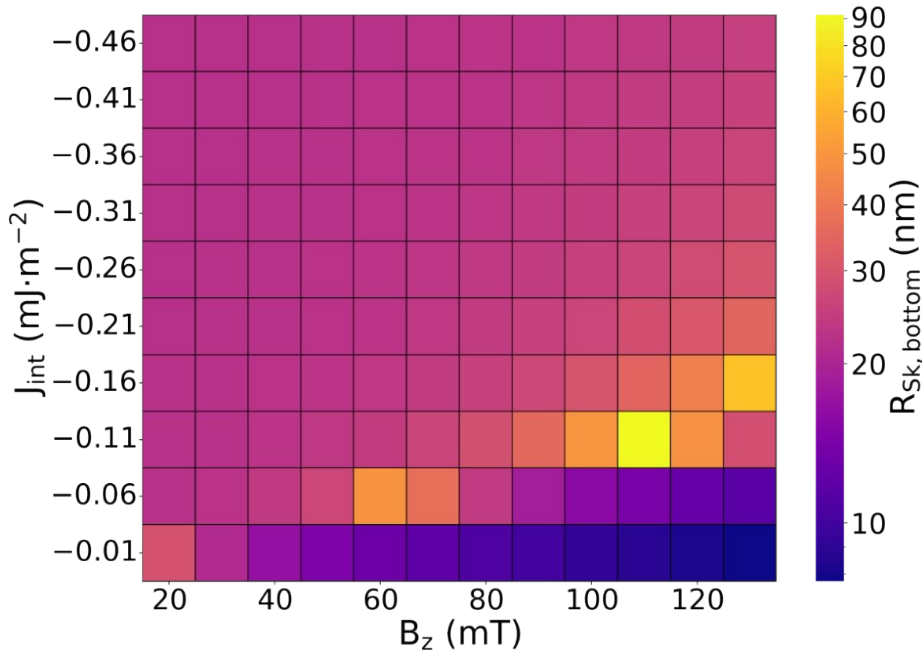
Figure S3. J_{int} and B_z effect on the SAF skyrmion radius (bottom interface).

3. SAF skyrmion radii phase diagram for M_{sat} and K_u with larger cell size:

Figure S4. SAF skyrmion radius for different values of M_{sat} and K_u for the SAF multilayer structure with in-plane cell size $c_x = c_y = 1$ nm.

4. Effect of polycrystallinity and sidewall roughness on skyrmion stability, pairing and propagation

The effect of variation in the magnitude and off-axis orientation of uniaxial anisotropy and sidewall roughness on skyrmion pairing and current-driven motion have been investigated. The following figures summarize the results for each parametric study:

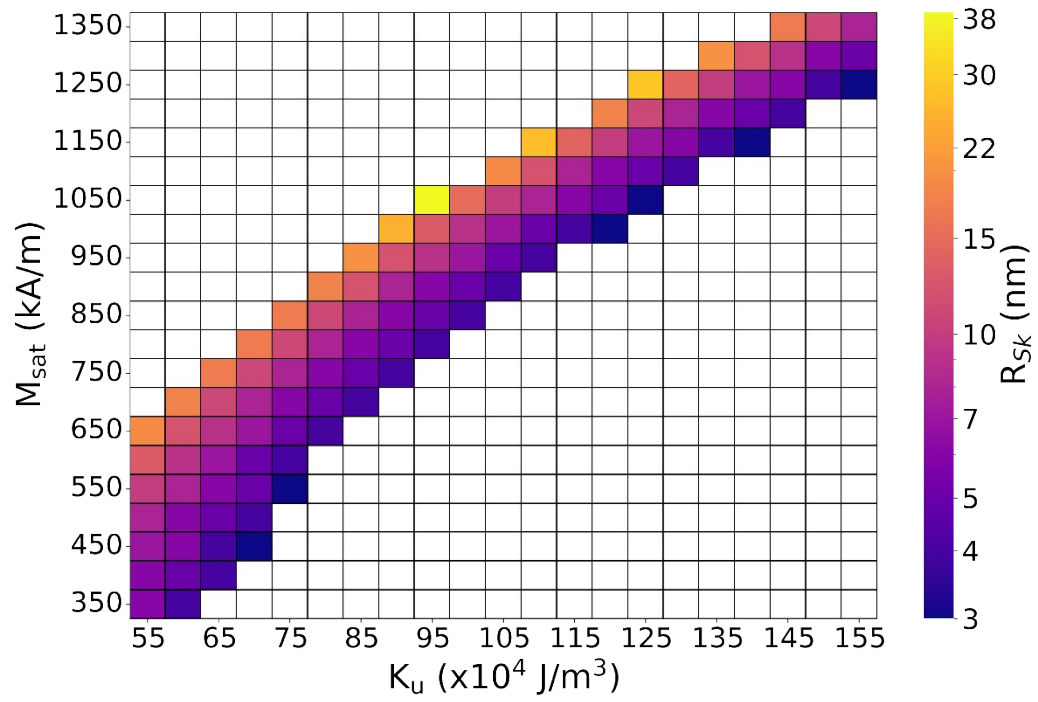**Effect of uniaxial anisotropy parameter difference on SAF skyrmion pairing and drive**
Supplementary Video V1. k_2_percent.out ($K_u^* = K_u^0 + \Delta K$, where $\Delta K \sim \mathcal{N}(0, 2\% \times K_u^0)$)
Supplementary Video V2. k_4_percent.out ($K_u^* = K_u^0 + \Delta K$, where $\Delta K \sim \mathcal{N}(0, 4\% \times K_u^0)$)
Supplementary Video V3. k_5_percent.out ($K_u^* = K_u^0 + \Delta K$, where $\Delta K \sim \mathcal{N}(0, 5\% \times K_u^0)$)
Supplementary Video V4. k_6_percent.out ($K_u^* = K_u^0 + \Delta K$, where $\Delta K \sim \mathcal{N}(0, 6\% \times K_u^0)$)

Effect of off-axis uniaxial anisotropy on SAF skyrmion pairing and drive
Supplementary Video V5. k_0_anis_0deg.out ($K_u^* = K_u$, not tilted for reference)
Supplementary Video V6. k_0_anis_1deg.out ($K_u^* = K_u$, Anisotropy axis tilted from Z axis by $\Delta\theta°$ where $\Delta\theta° \sim \mathcal{N}(0, 1^0)$)
Supplementary Video V7. k_0_anis_2deg.out ($K_u^* = K_u$, Anisotropy axis tilted from Z axis by $\Delta\theta°$ where $\Delta\theta° \sim \mathcal{N}(0, 2^0)$)
Supplementary Video V8. k_0_anis_3deg.out ($K_u^* = K_u$, Anisotropy axis tilted from Z axis by $\Delta\theta°$ where $\Delta\theta° \sim \mathcal{N}(0, 3^0)$)
Supplementary Video V9. k_0_anis_10deg.out ($K_u^* = K_u$, Anisotropy axis tilted from Z axis by $\Delta\theta°$ where $\Delta\theta° \sim \mathcal{N}(0, 10^0)$)

Sidewall roughness effects on SAF skyrmion pairing and drive
Supplementary Video V10. smooth.out (not sidewall roughness)
Supplementary Video V11. rough_edges10.out (sidewall roughness: $\mathcal{N}(0, 10\% \times \text{channel width})$)
Supplementary Video V12. rough_edges20.out (sidewall roughness: $\mathcal{N}(0, 20\% \times \text{channel width})$)
Supplementary Video V13. rough_edges40.out (sidewall roughness: $\mathcal{N}(0, 40\% \times \text{channel width})$)
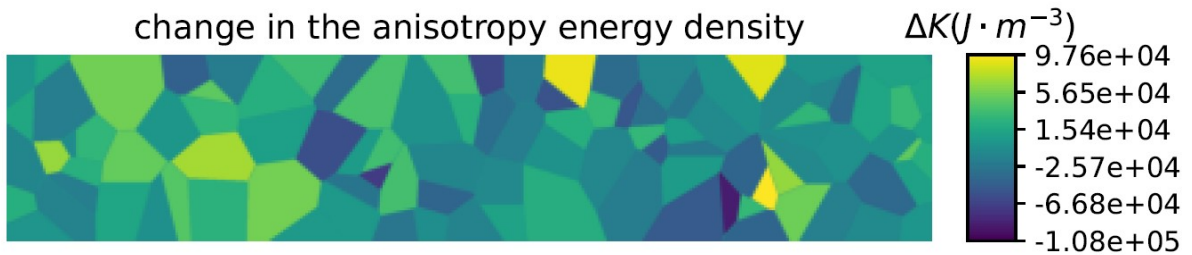

Figure S5. Example change in the anisotropy energy density (K_u) to model large variations among different grains in polycrystalline ferromagnetic layers. These variations directly affect skyrmion stability, coupling and drive current requirements and can act as pinning sites if the variation is high.
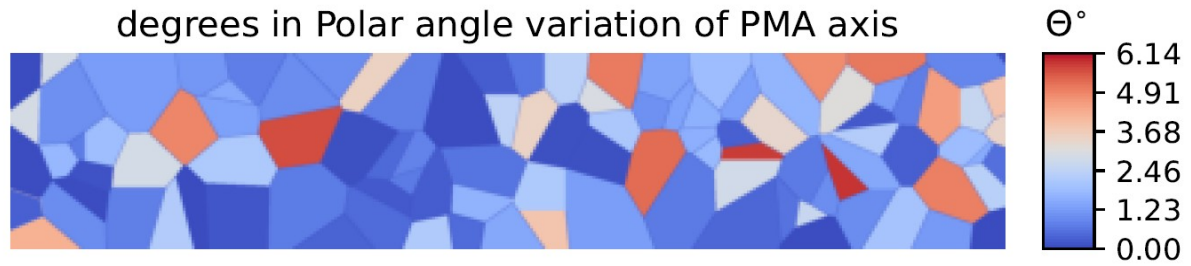
Figure S6. Example change in the polar angle of the perpendicular magnetic anisotropy direction to model large (or small) variations among different grains in polycrystalline ferromagnetic layers.
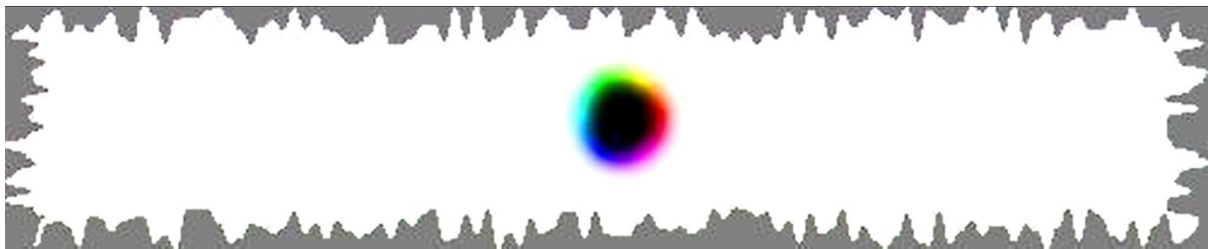
Figure S7. Effect of sidewall roughness on skyrmion stability and propagation. This example shows that random sidewall roughness with $3\sigma < 60\%$ of the channel widths of SAF multilayer slabs can sustain coupled skymions and their propagation.

Supplementary Videos and Their Discussion:

<u>**Effect of uniaxial anisotropy parameter difference on SAF skyrmion pairing and drive**</u>
Supplementary Video V1. k_2_percent.out ($K_u^* = K_u^0 + \Delta K$, where $\Delta K \sim \mathcal{N}(0, 2\% \times K_u^0)$)
Supplementary Video V2. k_4_percent.out ($K_u^* = K_u^0 + \Delta K$, where $\Delta K \sim \mathcal{N}(0, 4\% \times K_u^0)$)
Supplementary Video V3. k_5_percent.out ($K_u^* = K_u^0 + \Delta K$, where $\Delta K \sim \mathcal{N}(0, 5\% \times K_u^0)$)
Supplementary Video V4. k_6_percent.out ($K_u^* = K_u^0 + \Delta K$, where $\Delta K \sim \mathcal{N}(0, 6\% \times K_u^0)$)

<u>In the Supplementary Video V1,</u> the skyrmion pair wobbles due to the 2% uniaxial anisotropy variability across the polycrystalline grains. Despite this variability, skyrmion stability and operation at the same currents has not been hampered.

<u>In the Supplementary Video V2,</u> the skyrmion pair wobbles even more than the previous case due to the 4% uniaxial anisotropy variability across the polycrystalline grains. The SAF skyrmion pair is less stable and current control is near the edge of unpredictable operation. Despite this variability, skyrmion stability and operation at the same currents has not been hampered.

<u>In the Supplementary Videos V3 and V4,</u> the skyrmion pairs are pinned due to the larger uniaxial anisotropy variability across the adjacent polycrystalline grains (5 and 6%, respectively). Although SAF skyrmions are still stable, they cannot be driven with the same currents as in the first two cases anymore.

Effect of off-axis uniaxial anisotropy on SAF skyrmion pairing and drive
Supplementary Video V5. k_0_anis_0deg.out ($K_u^* = K_u$, not tilted for reference)
Supplementary Video V6. k_0_anis_1deg.out ($K_u^* = K_u$, Anisotropy axis tilted from Z axis by $\Delta\theta°$ where $\Delta\theta° \sim \mathcal{N}(0, 1^0)$)
Supplementary Video V7. k_0_anis_2deg.out ($K_u^* = K_u$, Anisotropy axis tilted from Z axis by $\Delta\theta°$ where $\Delta\theta° \sim \mathcal{N}(0, 2^0)$)
Supplementary Video V8. k_0_anis_3deg.out ($K_u^* = K_u$, Anisotropy axis tilted from Z axis by $\Delta\theta°$ where $\Delta\theta° \sim \mathcal{N}(0, 3^0)$)
Supplementary Video V9. k_0_anis_10deg.out ($K_u^* = K_u$, Anisotropy axis tilted from Z axis by $\Delta\theta°$ where $\Delta\theta° \sim \mathcal{N}(0, 10^0)$)

In the Supplementary Video V5, the skyrmion pair is driven without any barrier. This example is a reference case with no uniaxial anisotropy axis tilt (or 0° substrate miscut).

In the Supplementary Video V6, the skyrmion pair is driven with a wobbling motion. This example shows that even up to 1° uniaxial anisotropy axis tilt or variability across the polycrystal grains might cause significant instabilities.

In the Supplementary Video V7, the skyrmion pair is driven with a wobbling, expansion, and contraction motion. This example shows that up to 2° uniaxial anisotropy axis tilts or variabilities across the polycrystal grains might cause major instabilities.

In the Supplementary Video V8, the skyrmion pair is pinned due to the up to 3° variability of uniaxial anisotropy axis tilts across the polycrystal grains. This demonstration shows that the margin for uniaxial anisotropy variability across grains is very limited.

In the Supplementary Video V9, the skyrmion pair is pinned and grains also have different easy magnetization directions due to the up to 10° variability of uniaxial anisotropy axis tilts across the polycrystal grains. This demonstration shows that 10° variability must be avoided.

Sidewall roughness effects on SAF skyrmion pairing and drive
Supplementary Video V10. smooth.out (not sidewall roughness)
Supplementary Video V11. rough_edges10.out (sidewall roughness: $\mathcal{N}(0, 10\%\times$channel width))
Supplementary Video V12. rough_edges20.out (sidewall roughness: $\mathcal{N}(0, 20\%\times$channel width))
Supplementary Video V13. rough_edges40.out (sidewall roughness: $\mathcal{N}(0, 40\%\times$channel width))

In the Supplementary Video V10, this example shows the reference case without any sidewall roughness.

In the Supplementary Video V11, this case with 10% sidewall roughness shows that the demagnetizing fields here do not hinder the current-driven SAF skyrmion motion.

In the Supplementary Video V12, this case with 20% sidewall roughness shows that the demagnetizing fields here reduce the current-driven SAF skyrmion velocities, but do not completely block the skyrmion stability.

In the Supplementary Video V13, this case with 40% sidewall roughness shows that the demagnetizing fields completely prevent the stabilization of SAF skyrmions or pairs. This is due to the highly focused demagnetizing fields that prevent the equilibrium of SAF skyrmion effective anisotropy field terms.

5. MuMax3 example script of SAF skyrmion simulation

We used the code and parameters below generate and drive a coupled SAF skyrmion pair. The skyrmions are always much smaller than the simulation area ($2r = 50$ nm < 10% of the length of 1 side = 512 nm), the periodic boundary conditions do not cause any unintentional coupling between adjacent simulation regions. Simulations with both periodic boundary conditions and isolated skyrmions without periodic boundary conditions yielded the same equilibrium skyrmion results.

Parameter (unit)	Value
Saturation magnetization (M_{sat}, kA/m)	954.92965
DMI constant (D_{ind}, mJ/m^2)	2
Uniaxial anisotropy constant (K_u, kJ/m^3), along z	850
Intralayer exchange (A_{ex}, J/m)	10^{-11}
Gilbert damping (α)	0.1
Interlayer exchange interaction coefficient (J_{int}, mJ/m^2)	-0.13
Applied field (B_z, T)	0
Current density (J_e, A/m^2)	2.5×10^{11}
Hall angle	0.25
Spin-orbit torque χ and λ parameters (χ, λ)	(-2, 1)
Cell size (nm)	1
Simulation region (nm×nm)	512×512

```
Nx := 512
Ny := 512
setgridsize(Nx, Ny, 2)
c := 1e-9
cz := 1e-9
setcellsize(c, c, cz)
SetPBC(8, 8, 0)

defRegion(0, layer(0))
defRegion(1, layer(1))

// magnetic parameters for the SAF multilayers
Msat = 954929.65
Dind = 0.002
Ku1 = 850000.0
anisU = vector(0, 0, 1) // PMA
alpha = 0.1
Aex = 1e-11

RKKY := -0.00013
scale := (RKKY * cz) / (2 * Aex.Average())
ext_scaleExchange(0, 1, scale)

B_ext = vector(0, 0, 0) //applied B field

tableadd(ext_bubblepos)
tableadd(ext_bubbledist)

m.setRegion(0, neelskyrmion(1, -1).transl(-100e-9, 0, 0))
m.setRegion(1, neelskyrmion(-1, 1).transl(-100e-9, 0, 0)) //Neel type
sky charge(Qs)=-1, core mag = 1
minimize()
```

```
save(m)
snapshot(m)
TableSave()


//define constants and set slonczewksi parameters
SOTxi := -2
alphaH:= 0.25
Pol= alphaH
Lambda= 1
Epsilonprime= alphaH /2 * SOTxi
Fixedlayer= vector(1,0,0) //p
//define current
je := 2.5e11
J = vector(0,0,abs(-je))

autosave(m, 2e-10)
tableAutosave(2e-10)
run(2e-9)
snapshot(m)
```

6. Python code for output ovf files post processing

```python
# Loop through the directory of Ms and Ku sweeps, folders and files

# Specify the values for which we want to generate the scripts
Msat_values = [1e3*i for i in range(350,1400,50)] #sweep3
Ku_values = [1e4*i for i in range(55,160,5)]

results6 = []
for Msat in Msat_values:
    for Ku in Ku_values:
        #read a single ovf file produced after minimization
        ovffilePath = "MsKu_sweeps_p7/Ms_%02d/Ku_%g.out"%(Msat, Ku)
        if os.path.exists(ovffilePath):
            table, fields = read_ovf_out(ovffilePath)
            # Stack all snapshots of the magnetization on top of each
other
            m = np.stack([fields[key] for key in sorted(fields.keys())])
            ny = m.shape[3]
            cx = 0.25e-9 # cell size
            # Select the z component i = 2 acrross ny//2 at one z-layer
            mz  =  m[:,2,1,ny//2,:].T  #transpose  the  mz  array,
m[time,m_component,z_grid,y_grid,x_grid]
            #Check if there is one peak (skyrmion) or more (domain
strips)
            peaks, _ = find_peaks(mz.flatten(), width = (5,None))
            if (peaks.shape[0]>2 or peaks.shape[0]==0):
                print('at '+ovffilePath+' no skyrmion')
                results6.append( (Msat,Ku,np.nan) )
            else:
                # Read the data between skyrmion edges at mz=0 to
determine the diameter
                sky = np.where(mz>-0.25)[0]
                r = (sky.shape[0]*cx)/2 #get the radius of skyrmion
                results6.append( (Msat,Ku,r) )
```

```
        else:
            print('no directory found')

Msat6,Ku6,r6 = zip(*results6)
```

```
#Create a heatmap of relaxed skyrmion radius

r6_hm = np.asarray(r6).reshape(len(Msat_values),len(Ku_values))
fig, ax = plt.subplots(figsize=(15,10))

cbar_ticks = [ 1.25, 1.55, 2, 2.5, 3, 4, 5, 7, 10, 15, 22, 30, 38]
formatter = ticker.ScalarFormatter(useMathText=True)
formatter.set_scientific(False)

ax = sb.heatmap(r6_hm/1e-9, xticklabels = Ku_values, yticklabels =
Msat_values,
                cmap = 'plasma',
                #vmin = -60e-9/1e-9, vmax = 300-9/1e-9,
                #square = True,
                linewidth=0.5, linecolor='black',
                norm=LogNorm(),
                cbar_kws={'label': 'R$_{Sk}$ (nm)',
                        "ticks": cbar_ticks, "format": formatter,
                        #'ticks':ticker.MaxNLocator(nbins=20),
                        })

ax.set_yticklabels(["$%.0f$" % (y/1000) for y in Msat_values]);
ax.set_xticklabels(["$%.0f$" % (x/10000) for x in Ku_values], rotation
= 0);
plt.xlabel(r'K${\rm _u}$ (x$10^4$J$\cdot$ m$^{-3}$)', fontsize=30)
plt.ylabel(r'M$_{\rm sat}$ ( kA$\cdot$ m$^{-2}$)', fontsize=30)
plt.rcParams.update({'font.size': 25})
ax.figure.axes[-1].yaxis.label.set_size(30)

# Setting the number of ticks
plt.locator_params(axis='both', nbins=14)
ax.spines["right"].set_visible(True)
ax.spines["bottom"].set_visible(True)

ax.invert_yaxis()
plt.show()
```

References

1.   A. M. Cheghabouri and M. C. Onbasli, *Scientific Reports*, 2019, **9**, 9496.
2.   A. Mousavi Cheghabouri, F. Katmis and M. C. Onbasli, *Physical Review B*, 2022, **105**, 054411.

7. Materials options for SAF skyrmion implementation

Supplementary Table ST1 shows a list of materials options for FM/NM/FM layers and their respective references. The table shows the saturation magnetic moments, uniaxial anisotropy, and DMI constants

Material	M_s (kA/m)	K_u (kJ/m^3)	DMI (mJ/m^2)	Reference
Ta/Pt/CoFeB	700	400	1.5	[1]
Ta/CoFeB/MgO	600-1400	800	0.22	[2]–[4]
Ir/CoFeB/MgO	154	800	1.13	[5], [6]
Pt/CoFe/MgO	700	480	1.2	[7]
FePt	1150	1000 – 3000		[8], [9]
NdFeB	500 – 1000			[10]
NdFeCoB Alloy	530 – 1018			[11]
Pt/SmCo$_5$/Ta	640		1.47	[12]
Pt/SmCo$_5$/W	707		1.35	[12]
SmCo$_{7-x}$Ti$_x$	700 – 860			[13]
SmCo$_{7-x}$Cu$_x$	480 – 860			[14]
FeNi	1270	130		[15]

of the layers, which were simulation in the main manuscript. Since not all references document the interlayer exchange, the skyrmion coupling strengths achievable with these layers might vary in the experiments. Given the window of interlayer exchange values studied in the model in Figure 4 in the main manuscript, weak interlayer exchange values might as well be sufficient to stabilize the SAF skyrmion pairs in many real materials listed below.

Fe-Co-Ni-Cr-Al-Si Thin Films	900			[16]
Cr/Fe/MgO	900	609		[17]
[Ir/Co/Pt]$_x$	960	749		[18]
FeCoNi Alloy	310 – 1034			[19]

Supplementary Table ST1. Suggested list of magnetic materials that fall in the range of M_s, K_u, and D_{ind}, specified in Figures 2 and 3 of the main manuscript.

[1] Y. Zhou, R. Mansell, S. Valencia, F. Kronast, and S. van Dijken, "Temperature dependence of the Dzyaloshinskii-Moriya interaction in ultrathin films," *Phys Rev B*, vol. 101, no. 5, p. 054433, Feb. 2020, doi: 10.1103/PhysRevB.101.054433.

[2] S. Iihama, S. Mizukami, H. Naganuma, M. Oogane, Y. Ando, and T. Miyazaki, "Gilbert damping constants of Ta/CoFeB/MgO(Ta) thin films measured by optical detection of precessional magnetization dynamics," *Phys Rev B*, vol. 89, no. 17, p. 174416, May 2014, doi: 10.1103/PhysRevB.89.174416.

[3] T. Devolder, J. V. Kim, L. Nistor, R. Sousa, B. Rodmacq, and B. Diény, "Exchange stiffness in ultrathin perpendicularly magnetized CoFeB layers determined using the spectroscopy of electrically excited spin waves," *J Appl Phys*, vol. 120, no. 18, p. 183902, Nov. 2016, doi: 10.1063/1.4967826/143038.

[4] J. Cao *et al.*, "Spin orbit torques induced magnetization reversal through asymmetric domain wall propagation in Ta/CoFeB/MgO structures," *Sci Rep*, vol. 8, no. 1, p. 1355, Jan. 2018, doi: 10.1038/s41598-018-19927-5.

[5] W. Skowroński *et al.*, "Perpendicular magnetic anisotropy of Ir/CoFeB/MgO trilayer system tuned by electric fields," *Applied Physics Express*, vol. 8, no. 5, p. 053003, May 2015, doi: 10.7567/APEX.8.053003/XML.

[6] R. Chen *et al.*, "Large Dzyaloshinskii-Moriya interaction and room-temperature nanoscale skyrmions in CoFeB/MgO heterostructures," *Cell Rep Phys Sci*, vol. 2, no. 11, p. 100618, Nov. 2021, doi: 10.1016/j.xcrp.2021.100618.

[7] S. Emori *et al.*, "Spin Hall torque magnetometry of Dzyaloshinskii domain walls," *Phys Rev B*, vol. 90, no. 18, p. 184427, Nov. 2014, doi: 10.1103/PhysRevB.90.184427.

[8] W. Zhou, T. Seki, H. Arai, H. Imamura, and K. Takanashi, "Vortex-dynamics-mediated low-field magnetization switching in an exchange-coupled system," *Phys Rev B*, vol. 94, no. 22, p. 220401, Dec. 2016, doi: 10.1103/PhysRevB.94.220401.

[9]   T. Ono, N. Kikuchi, S. Okamoto, O. Kitakami, and T. Shimatsu, "Novel torque magnetometry for uniaxial anisotropy constants of thin films and its application to FePt granular thin films," *Applied Physics Express*, vol. 11, no. 3, p. 033002, Mar. 2018, doi: 10.7567/APEX.11.033002.

[10]   S. N. Piramanayagam, M. Matsumoto, A. Morisako, and S. Takei, "Studies on NdFeB thin films over a wide composition range," *J Alloys Compd*, vol. 281, no. 1, pp. 27–31, Nov. 1998, doi: 10.1016/S0925-8388(98)00765-8.

[11]   B. Mirtaheri and H. Tahanian, "Advances in Developing Permanent Magnets with Less or No Rare-Earth Elements," *Electromechanical Energy Conversion Systems*, vol. 2, no. 1, pp. 52–69, Jan. 2022, doi: 10.30503/EECS.2022.166814.

[12]   H. Zhou *et al.*, "Rare-Earth Permanent Magnet SmCo5 for Chiral Interfacial Spin-Orbitronics," *Adv Funct Mater*, vol. 31, no. 46, p. 2104426, Nov. 2021, doi: 10.1002/adfm.202104426.

[13]   J. Zhou, I. A. Al-Omari, J. P. Liu, and D. J. Sellmyer, "Structure and magnetic properties of SmCo7−xTix with TbCu7-type structure," *J Appl Phys*, vol. 87, no. 9, pp. 5299–5301, May 2000, doi: 10.1063/1.373327.

[14]   I. A. Al-Omari, Y. Yeshurun, J. Zhou, and D. J. Sellmyer, "Magnetic and structural properties of SmCo7−xCux alloys," *J Appl Phys*, vol. 87, no. 9, pp. 6710–6712, May 2000, doi: 10.1063/1.372816.

[15]   B. Mirtaheri and H. Tahanian, "Advances in Developing Permanent Magnets with Less or No Rare-Earth Elements," *Electromechanical Energy Conversion Systems*, vol. 2, no. 1, pp. 52–69, Jan. 2022, doi: 10.30503/eecs.2022.166814.

[16]   P.-C. Lin, C.-Y. Cheng, J.-W. Yeh, and T.-S. Chin, "Soft Magnetic Properties of High-Entropy Fe-Co-Ni-Cr-Al-Si Thin Films," *Entropy*, vol. 18, no. 8, p. 308, Aug. 2016, doi: 10.3390/e18080308.

[17]   A. Kozioł-Rachwał, T. Nozaki, K. Freindl, J. Korecki, S. Yuasa, and Y. Suzuki, "Enhancement of perpendicular magnetic anisotropy and its electric field-induced change through interface engineering in Cr/Fe/MgO," *Sci Rep*, vol. 7, no. 1, p. 5993, Jul. 2017, doi: 10.1038/s41598-017-05994-7.

[18]   C. Moreau-Luchaire *et al.*, "Additive interfacial chiral interaction in multilayers for stabilization of small individual skyrmions at room temperature," *Nat Nanotechnol*, vol. 11, no. 5, pp. 444–448, May 2016, doi: 10.1038/nnano.2015.313.

[19]   Y. Zhang, T. Zuo, Y. Cheng, and P. K. Liaw, "High-entropy Alloys with High Saturation Magnetization, Electrical Resistivity and Malleability," *Sci Rep*, vol. 3, no. 1, p. 1455, Mar. 2013, doi: 10.1038/srep01455.

8. Comparison of Spin-orbit Torques and Spin Transfer Torques in the SAF skyrmion velocities

We developed a micromagnetic model for both SOT and STT configurations separately. The current dependence of the circuit is shown below. For low external magnetic fields below about 100 mT, SOT provides lower SAF skyrmion velocity, while above this field, SOT starts yielding faster SAF velocities. We attribute this behavior to the increasing field-like torques in SOT under external magnetic field, while external magnetic field does not have a sizable effect on the STT-driven SAF skyrmion velocities.